

# Air-Sea Turbulent Heat Flux Feedback over Mesoscale Eddies

Sophia Moreton<sup>1</sup>, David Ferreira<sup>1</sup>, Malcolm Roberts<sup>2</sup>, Helene Hewitt<sup>2</sup>

<sup>1</sup>University of Reading, UK

<sup>2</sup>UK Met Office Hadley Centre, Exeter, UK

## Key Points:

- Global turbulent heat flux feedback over coherent mesoscale eddies ranges between 35-45 W m<sup>-2</sup> K<sup>-1</sup>
- Ocean to atmosphere SST regriding can underestimate turbulent heat flux feedback by up to 75%
- Coupled models need a coordinated increase in ocean and atmosphere resolutions

---

Corresponding author: Sophia Moreton, [s.moreton@pgr.reading.ac.uk](mailto:s.moreton@pgr.reading.ac.uk)

12 **Abstract**

13 Air-sea turbulent heat fluxes play a fundamental role in generating and dampen-  
 14 ing sea surface temperature (SST) anomalies. To date, the turbulent heat flux feedback  
 15 (THFF) is well quantified at basin-wide scales ( $\sim 20 \text{ W m}^{-2} \text{ K}^{-1}$ ) but remains unknown  
 16 at the oceanic mesoscale (10-100 km). Here, using an eddy-tracking algorithm in three  
 17 configurations of the coupled climate model HadGEM3-GC3.1, the THFF over mesoscale  
 18 eddies is estimated. The THFF magnitude is strongly dependent on the ocean-to-atmosphere  
 19 regriding of SST, a common practice in coupled models for calculating air-sea heat flux.  
 20 Our best estimate shows that the mesoscale THFF ranges between 35 and 45  $\text{W m}^{-2} \text{ K}^{-1}$   
 21 globally, across different eddy amplitudes. Increasing the ratio of atmosphere-to-ocean  
 22 grid resolution can lead to an underestimation of the THFF, by as much as 75% for a  
 23 6:1 resolution ratio. Our results suggest that a large atmosphere-to-ocean grid ratio can  
 24 result in an artificially weak dampening of mesoscale SST anomalies.

25 Plain language summary: Sea surface temperature (SST) anomalies are vital for  
 26 both regulating the earth's weather and climate. The generation and reduction of these  
 27 SST anomalies is largely determined by air-sea heat fluxes, particularly turbulent (la-  
 28 tent and sensible) heat fluxes. So far in current research, the feedback from these tur-  
 29 bulent heat fluxes is well known at large scales, i.e. over the whole ocean basin. How-  
 30 ever, a quantification of this feedback at much smaller spatial scales (10-100 km) over  
 31 individual mesoscale ocean eddies is still missing. Due to the availability of high reso-  
 32 lution data from a coupled climate model, this study provides the first global estimate  
 33 of this feedback over individually tracked and averaged mesoscale eddies. The estimate  
 34 ranges between 35 to 45  $\text{W m}^{-2} \text{ K}^{-1}$ , depending on an eddy's sea surface height anomaly.  
 35 In coupled climate models, if the spatial resolution of the atmospheric grid is much larger  
 36 than the ocean grid resolution, with a ratio 6:1, a 75% underestimation of this feedback  
 37 occurs. This massive underestimation suggests, in this model, SST anomalies within mesoscale  
 38 eddies are not reduced enough by air-sea heat fluxes, and consequently will remain too  
 39 large.

40 **1 Introduction**

41 The turbulent heat flux feedback (THFF, in  $\text{W m}^{-2} \text{ K}^{-1}$ , denoted  $\alpha$  hereafter) is  
 42 a critical parameter, which measures the change in the net air-sea turbulent heat flux  
 43 in response to a 1 K change in sea surface temperature (SST). It is a powerful tool to  
 44 quantify the rate of dampening of SST anomalies. THFF can vary seasonally (largest  
 45 in winter), geographically and with ocean spatial scale. Early studies estimate THFF

46 at approximately  $20 \text{ W m}^{-2} \text{ K}^{-1}$  for basin-scale mid-latitude SST anomalies, which, to  
47 first order, respond passively to atmospheric forcing (Bretherton, 1982; Frankignoul, 1985;  
48 Frankignoul, Czaja, & L'Heveder, 1998; Frankignoul et al., 2004; Small, Bryan, Bishop,  
49 Larson, & Tomas, 2020). More recent studies estimate that THFF increases to  $40 \text{ W m}^{-2} \text{ K}^{-1}$   
50 in the Gulf Stream, and decreases down to  $10 \text{ W m}^{-2} \text{ K}^{-1}$  in the Antarctic Circumpo-  
51 lar Current (Hausmann & Czaja, 2012; Hausmann, Czaja, & Marshall, 2017). To date,  
52 while THFF is known to increase towards smaller scales, the smallest spatial scale used  
53 to quantify THFF is approximately 100 km.

54 The magnitude of THFF depends on the background SST and the adjustment of  
55 the atmospheric boundary layer (ABL) to the SST anomaly. It is suggested that the re-  
56 moval of heat by surface winds is a key process (Bretherton, 1982; Hausmann, Czaja,  
57 & Marshall, 2016). On smaller scales, heat can easily be advected away from the SST  
58 anomaly, maintaining a large air-sea temperature contrast and strong heat flux damp-  
59 ing. While on basin scales, this process becomes less efficient (slower), resulting in a small  
60 temperature contrast and large damping. On global scale, this adjustment completely  
61 disappears: the heat removal is controlled by radiation out to space and the THFF reaches  
62 only about  $1\text{-}2 \text{ W m}^{-2} \text{ K}^{-1}$  (Gregory et al., 2004). However, how the THFF behaves at  
63 spatial scales below 100 km remains unknown.

64 Formed through intrinsic ocean variability, mesoscale eddy SST anomalies (of ra-  
65 dius 10-100 km) drive distinct changes within the ABL through the so-called 'vertical  
66 mixing mechanism' (Frenger, Gruber, Knutti, & Münnich, 2013; Hayes, McPhaden, &  
67 Wallace, 1989; Putrasahan, Miller, & Seo, 2013; Small, Bryan, Bishop, & Tomas, 2019;  
68 Wallace, Mitchell, & Deser, 1989). A warm mesoscale SST anomaly transfers heat through  
69 turbulent heat fluxes up into the ABL, which increases local vertical mixing, reduces sta-  
70 bility and extends the height of the ABL. The increase in mixing encourages the trans-  
71 fer of momentum downwards and strengthens surface winds, cloud cover and rainfall.  
72 The opposite occurs over a cold SST anomaly. Past research on mesoscale air-sea exchanges  
73 largely focuses on momentum fluxes however in eddy-rich regions, mesoscale-induced air-  
74 sea turbulent heat fluxes play an important role in altering eddy kinetic and potential  
75 energy and dampening SST anomalies (Bishop, Small, & Bryan, 2020; Hogg, Dewar, Berloff,  
76 Kravtsov, & Hutchinson, 2009; Renault, Marchesiello, Masson, & McWilliams, 2019; Re-  
77 nault et al., 2016; Seo, Miller, & Norris, 2016). Furthermore, mesoscale SST-turbulent  
78 heat flux exchanges can strengthen western boundary currents (WBC) by 20 to 40% and  
79 weaken thermal stratification in the upper ocean (Ma et al., 2016; Shan et al., 2020; Small  
80 et al., 2020). It is therefore important to provide a quantification of THFF over tran-  
81 sient mesoscale eddies.

82 Observational estimates of THFF at the oceanic mesoscale are restricted by the  
83 availability of high-resolution ocean and atmosphere data. First, the consistency and ef-  
84 fective resolution of global air-sea heat flux datasets are questionable, due to the differ-  
85 ent space-time resolutions from either atmospheric reanalysis or satellites (Cronin et al.,  
86 2019; Leyba, Saraceno, & Solman, 2016; Li, Sang, & Jing, 2017; Villas Bôas, Sato, Chaigneau,  
87 & Castelão, 2015). Second, radii of mesoscale eddies, estimated from gridded sea sur-  
88 face height product such as AVISO [Archiving, Validation and Interpolating of Satellite  
89 Oceanographic Data, 2014] maybe be overestimated by a factor of 2 due to the interpo-  
90 lation of raw satellite tracks needed to create a gridded product (Chelton, 2013; Cronin  
91 et al., 2019; Ducet, Le Traon, & Reverdin, 2000; Hausmann & Czaja, 2012; Minobe, Kuwano-  
92 Yoshida, Komori, Xie, & Small, 2008; Moreton, Ferreira, Roberts, & Hewitt, 2020; Small  
93 et al., 2008; Xie, 2004). As a result, this study uses a global coupled climate model with  
94 higher spatial ocean and atmospheric resolution than currently available in observations.

95 Current state-of-the-art climate models can provide global eddy-rich ocean simu-  
96 lations, with a horizontal resolution of approximately  $1/12^\circ$ . At this resolution, mesoscale  
97 eddies can be explicitly resolved globally, except in the highest latitudes with more, smaller  
98 and longer-lasting eddies compared to a  $1/4^\circ$  resolution (Haarsma et al., 2016; Hewitt  
99 et al., 2017; Moreton et al., 2020; M. J. Roberts et al., 2019). However, whether an eddy-  
100 rich ocean results in an improved representation of mesoscale SST-turbulent heat flux  
101 exchanges remains to be determined. The ratio of ocean-atmosphere horizontal resolu-  
102 tion is likely to be an important factor (Jullien et al., 2020). In many current high-resolution  
103 coupled models, with the exception of the Community Earth System Model (CESM),  
104 air-sea fluxes are computed on the atmospheric grid, which requires the interpolation of  
105 SST from the oceanic grid to the often coarser atmospheric grid (Yang, Jing, & Wu, 2018).  
106 The interpolation is likely to smooth out mesoscale features resolved on the ocean grid  
107 before calculation of the air-sea exchanges and if so, to introduce significant biases in air-  
108 sea feedbacks.

109 Therefore, the following study has two goals: 1) to provide the first estimate of THFF  
110 over coherent mesoscale eddies globally at smaller spatial scales than previously evalu-  
111 ated and 2), to evaluate if THFF is dependent on the ratio of ocean-atmosphere reso-  
112 lution in coupled models. The three configurations of a high-resolution coupled climate  
113 model, and the methods to compute and rationalize THFF at the mesoscale are intro-  
114 duced in section 2. Section 3 presents the results addressing the two goals, and finally  
115 section 4 concludes and discusses implications for future research and model development.

## 116 2 Materials and Methods

### 117 2.1 Model data

118 The following results use output from the high-resolution global coupled climate  
 119 model, HadGEM3-GC3.1 (Williams et al., 2018). The climate model couples an atmo-  
 120 sphere (MetUM), land (JULES), ocean (NEMO) and sea ice (CICE) components (Madec,  
 121 2008; Storkey et al., 2018; Walters et al., 2017). The model simulations follow the CMIP6  
 122 HighResMIP protocol, as part of PRIMAVERA (Haarsma et al., 2016; M. J. Roberts  
 123 et al., 2019). Three configurations of this model are compared, with a different ratio of  
 124 ocean-atmosphere resolution: N512-12 ( $\sim 25$  km atmosphere,  $1/12^\circ$  ocean), N216-12 ( $\sim 60$  km  
 125 atmosphere,  $1/12^\circ$  ocean) and finally, N216-025 ( $\sim 60$  km atmosphere,  $1/4^\circ$  ocean). Model  
 126 outputs are obtained after a 20-year spin-up, and one year of daily data is used (the re-  
 127 sults are independent of the year chosen).

128 To compute air-sea turbulent (latent and sensible) heat fluxes (THFs), the OASIS3  
 129 coupler passes the ocean model SST to the atmospheric grid using a second-order con-  
 130 servative interpolation (Hewitt et al., 2011; Valcke, 2013; Valcke, Craig, & L., 2015). In  
 131 the following, the SST on the ocean grid ( $SST_O$ ) is distinguished from the regridded SST  
 132 on the atmospheric grid ( $SST_A$ ). Positive values of THF denote fluxes upwards from the  
 133 ocean to the atmosphere. Finally, surface air temperature is taken at 1.5 m.

### 134 2.2 Eddy tracking and compositing

135 Closed coherent mesoscale eddies are identified and tracked daily in the global ocean  
 136 for 20 years from sea surface height (SSH), using an eddy tracking algorithm. The al-  
 137 gorithm is adapted from Mason, Pascual, and McWilliams (2014) and Chelton, Schlax,  
 138 and Samelson (2011). As well as being dependent on SSH contours, an eddy is tracked  
 139 subject to certain criteria, such as a shape test or pixel number. The algorithm is de-  
 140 scribed in detail in Moreton et al. (2020). A discussion of the eddy characteristics and  
 141 comparison of the model with the AVISO satellite product is also provided by Moreton  
 142 et al. (2020).

143 To isolate mesoscale anomalies, a 10-year climatological mean is removed from the  
 144 fields which are subsequently high-pass filtered (using the same filter as for eddy track-  
 145 ing, see SPM for details). Following Frenger et al. (2013); Hausmann and Czaja (2012);  
 146 Villas Bôas et al. (2015), 'composite averaging' is used to remove high-frequency vari-  
 147 ability associated with weather (shown in Fig. 1 from N512-12), as follows. High-pass  
 148 filtered anomalies centered on each eddy are normalized by the effective eddy radius ( $L_{eff}$ )  
 149 and averaged for all eddies globally.  $L_{eff}$  is defined as the radius of a fitted circle with

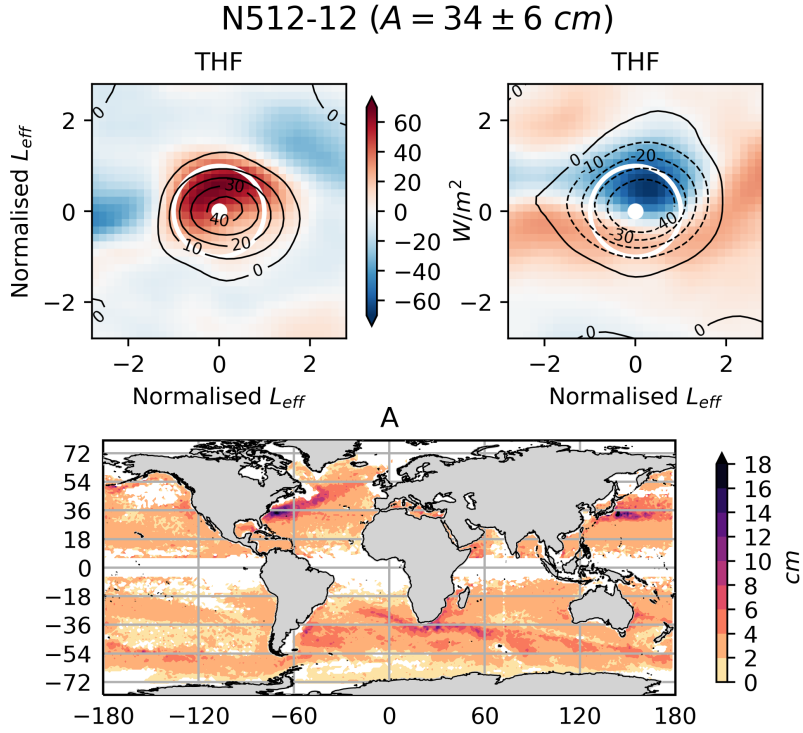


**Figure 1.** Composite maps of turbulent heat flux THF (colour shading, in  $\text{W m}^{-2}$ ) and SSH (black lines, in cm) for large-amplitude ( $A=34\pm 6$  cm) anti-cyclonic (upper left) and cyclonic (upper right) eddies from N512-12. Solid (dashed) lines indicate positive (negative) values. The white dot is the centre of each tracked eddy and the white circle is 1 effective eddy radius ( $L_{eff}$ ). (bottom panel) The map is eddy amplitude ( $A$ , in cm) binned into a  $1^\circ$  grid from the tracked eddies in N512-12.

150 the same area as the outermost closed SSH contour in each tracked eddy. Composites  
 151 are plotted in units of  $L_{eff}$ . Rotating the anomalies (to align with background SST or  
 152 wind direction) before averaging was found to make little difference to the results.

153 Finally, the eddies and their associated fields are binned according to their eddy  
 154 amplitude ( $A$ ) from  $1\pm 0.05$  cm to  $34\pm 6$  cm. A global map of the averaged eddy ampli-  
 155 tude per  $1^\circ$  squared is shown in Fig. 1. As expected, larger amplitude eddies are con-  
 156 centrated in eddy-rich regions, such as WBCs and the Southern Ocean.  $A$  is the abso-  
 157 lute difference between either the maximum (for anti-cyclones) or minimum (cyclones)  
 158 SSH and the SSH magnitude at the outermost closed SSH contour of the tracked eddy.  
 159 This means the SSH anomaly is larger than eddy amplitude and can extend spatially be-  
 160 yond the tracked eddy radius (Fig. 1). It should be highlighted that eddy amplitude and

161 eddy radius are not strongly related (Chelton et al., 2011; Moreton et al., 2020). Instead,  
 162 eddy amplitude is linearly related to SST anomalies, especially for  $A \leq 25$  cm, shown  
 163 in SPM Fig. S3 B,C, as found in previous studies (Villas Bôas et al., 2015).

164 An accurate comparison of eddy composites from the model to observations is dif-  
 165 ficult, due to the coarser resolution found in observations and differences in either how  
 166 the SSH anomalies are isolated (i.e. by standard deviation of SSHA or eddy tracking),  
 167 the eddy tracking algorithm or in the strength of the high-pass filtering. However, the  
 168  $SST_O$  composites in the model (maximum of 0.5-0.6 K using binned eddy amplitudes  
 169 of 15 cm) and in a previous observational study (0.7 K) have similar magnitudes and spa-  
 170 tial distributions, i.e. a monopole for larger amplitude or a dipole for smaller amplitude  
 171 eddies (Hausmann & Czaja, 2012). Larger differences between the model and observa-  
 172 tions are found for LHF anomalies, especially at larger amplitudes (20-30 cm): N512-  
 173 12 has a maximum LHF anomaly of  $32 \text{ W m}^{-2} \text{ K}^{-1}$ , whilst only  $5-7 \text{ W m}^{-2} \text{ K}^{-1}$  in ob-  
 174 servations (Villas Bôas et al., 2015).

### 175 **2.3 Decomposition of the turbulent heat flux feedback**

176 The THFF  $\alpha$  is defined as:

$$\langle THF' \rangle = \alpha \langle SST' \rangle \quad (1)$$

177 where primes indicate the high-pass filtered anomalies, and  $\langle . \rangle$  indicates the com-  
 178 posite averaging over all eddies. A positive value of  $\alpha$  represents a negative heat flux feed-  
 179 back, i.e. a dampening of the SST anomaly by turbulent heat fluxes.

180 Due to the regridding of SST to calculate air-sea heat fluxes in the coupled model,  
 181 two THFFs can be computed from either  $SST_A$  or  $SST_O$ :

$$\langle THF' \rangle = \alpha_O \langle SST'_O \rangle \quad (2)$$

$$\langle THF' \rangle = \alpha_A \langle SST'_A \rangle. \quad (3)$$

182 The THFF  $\alpha_O$  relates the THF anomalies to the prognostic SST anomalies in the ocean  
 183 component, while  $\alpha_A$  represents the THFF after re-gridding the ocean grid SST to the  
 184 atmospheric grid ( $SST_A$ ). Note that  $\alpha_A$  does not affect directly the prognostic state of  
 185 the simulation. By isolating THFF based on  $SST_O$  ( $\alpha_O$ ) or based on re-gridded SST ( $\alpha_A$ ),  
 186 we can provide an estimate for how the THFF is affected by the ratio of ocean-atmosphere  
 187 resolution in coupled models.

188 To understand the behaviour of the THFFs  $\alpha_O$  and  $\alpha_A$ , it is useful to introduce  
 189 three coefficients  $\lambda_A$ ,  $\delta$  and  $R_g$  (Eqs. 4-6 below). First, the THF restoring coefficient  $\lambda_A$   
 190 is a simplification of the latent and sensible heat flux (LHF and SHF) bulk formulae used

191 in the model (Large & Yeager, 2004). Following Frankignoul et al. (1998) and Hausmann  
 192 et al. (2017)), we assume that the LHF can be linearized to be expressed in terms of the  
 193 air-sea temperature difference,  $T_{air} - SST_A$ . Second,  $\delta$  measures the adjustment of the  
 194 surface air temperature  $T_{air}$  to the regrided SST anomalies  $SST_A$ : when  $\delta$  equals zero  
 195 there is no ABL response or adjustment, whilst when  $\delta$  equals one, a complete adjust-  
 196 ment occurs resulting in a zero THF. Third, the  $R_g$  coefficient measures the impact of  
 197 the ocean-to-atmosphere regriding on the SST magnitude. If  $R_g$  equals one, the mag-  
 198 nitude of the SST anomalies is preserved during the regriding.

$$\langle THF' \rangle = \lambda_A (\langle SST'_A \rangle - \langle T'_{air} \rangle) \quad (4)$$

$$\langle T'_{air} \rangle = \delta \langle SST'_A \rangle \quad (5)$$

$$\langle SST'_A \rangle = R_g \langle SST'_O \rangle . \quad (6)$$

199 By re-arranging, relationships between the coefficients can be derived, in order to  
 200 trace changes from the THF restoring coefficient  $\lambda_A$  to  $\alpha_O$ :

$$\alpha_A = (1 - \delta) \lambda_A \quad (7)$$

$$\alpha_O = R_g \alpha_A \quad (8)$$

201 The THFF  $\alpha_A$  is scaled down from  $\lambda_A$  by the air temperature adjustment in the  
 202 ABL (Eq. 7). When the ABL temperature adjustment is weak (i.e.  $\delta \sim 0$ ),  $\alpha_A$  is close  
 203 to the restoring embedded in the THF bulk formulae (i.e.  $\lambda_A$  here). Whilst when the  
 204 adjustment is strong, the THFF  $\alpha_A$ , and subsequently the dampening of SST anoma-  
 205 lies, is much smaller than predicted by  $\lambda_A$  (Frankignoul et al., 1998). In other words,  
 206 the coefficient  $\lambda_A$  represents an upper bound for  $\alpha_A$ , which is achieved when air tem-  
 207 perature adjustment ( $\delta$ ) is zero. This upper bound is the "fast limit" discussed by Haus-  
 208 mann et al. (2017).

209 The THFF using ocean model SST ( $\alpha_O$ ) is reduced from  $\alpha_a$  by the SST regriding  
 210 coefficient  $R_g$  (Eq. 8). It is anticipated that  $R_g$  is smaller than one and therefore  $\alpha_O$  is  
 211 biased low compared to  $\alpha_A$ .

212 In practice, the above coefficients are estimated over coherent mesoscale eddies through  
 213 a linear regression between the points of the composite maps (see Fig. 2). Since SST,  
 214  $T_{air}$  and THF anomalies tend to extend outside the eddy radius, points up to  $\pm 2.8$  times  
 215 the eddy radius are included in the linear regression. Regressions for anti-cyclonic and  
 216 cyclonic eddies are calculated separately, and a weighted average is used to produce a  
 217 total value (given as text in Fig. 2). The gradients of linear regression are dependent on  
 218  $SST_{O/A}$  being on the  $x - axis$ .

### 219 3 Results

220 First the THFF coefficients,  $\alpha_A$  and  $\alpha_O$ , are discussed for the N512-12 configura-  
 221 tion, which is the least affected by regridding biases (section 3.1). A comparison to N216-  
 222 12 and N216-025 configurations follows, to evaluate the impact of changes in the ratio  
 223 of ocean-atmosphere resolutions on the THFF (section 3.2).

#### 224 3.1 Estimating THFF over large-amplitude mesoscale eddies

225 Fig. 2 illustrates the relationships between the composite fields for the large am-  
 226 plitude eddies ( $A=34\pm 6$  cm) globally in N512-12. A repeat of the relationships for small-  
 227 amplitude mesoscale eddies ( $A=1\pm 0.05$  cm) can be found in the Appendix (Fig. S1). The  
 228 estimated coefficients  $\alpha_{O/A}$ ,  $\lambda_A$ ,  $\delta$  and  $R_g$  from Eqs. (2)-(6) are indicated in each panel  
 229 with error bars.

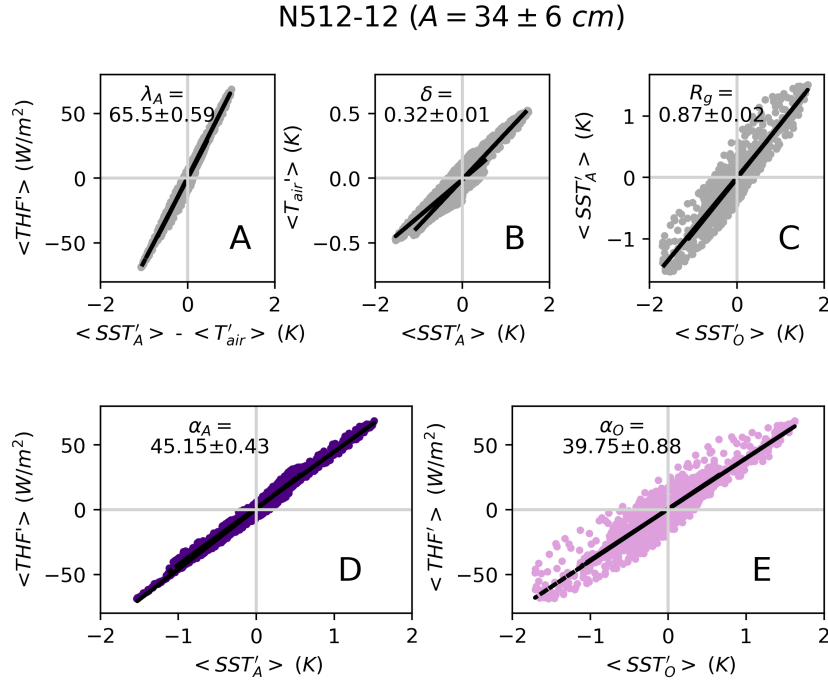


**Figure 2.** Relationships between the composite fields of  $SST_{O/A}$ , THF and  $T_{air}$ , with the estimated coefficients ( $\alpha_{O/A}$ ,  $\lambda_A$ ,  $\delta$  and  $R_g$ ) for the larger amplitude eddies ( $A=34\pm 6$  cm) globally in N512-12. The coefficients are given by gradient of the linear regression line (black) +/- the 95% confidence interval.

230 There is a strong linear relationship between the composite anomalies of THF and  
 231 air-sea temperature contrast (Fig. 2A), providing a robust estimate of  $\lambda_A$  at  $65.5\pm 0.59$   $\text{W m}^{-2} \text{K}^{-1}$ .

232 This is larger than previous estimates of about  $50 \text{ W m}^{-2} \text{ K}^{-1}$  (Frankignoul et al., 1998;  
 233 Rahmstorf & Willebrand, 1995) and the upper bound of  $25\text{-}35 \text{ W m}^{-2} \text{ K}^{-1}$  of Hausmann  
 234 et al. (2017). This discrepancy could reflect differences in the estimation methods. Pub-  
 235 lished estimates are based on the linearization of bulk formulae using constant drag co-  
 236 efficients and monthly-mean large-scale winds. In contrast, our estimates (Fig. 2A) im-  
 237 plicitly account for 1) the full complexity of the bulk formulae implemented in HadGEM3-  
 238 GC3.1, where the drag coefficient is function of ABL stability and surface winds (He-  
 239 witt et al., 2011) and 2) dynamical adjustments in the ABL such as the modulation of  
 240 surface winds by mesoscale eddy SST anomalies (Frenger et al., 2013; M. J. Roberts et  
 241 al., 2016).

242 The atmospheric adjustment parameter  $\delta$  is estimated at  $0.32 \pm 0.01$  for large am-  
 243 plitude eddies globally (Fig. 2B), i.e. the surface air temperature  $T_{air}$  anomaly is about  
 244 a third of the mesoscale SST anomaly. Previous studies give 0.5 in the WBCs and the  
 245 Antarctic Circumpolar Current (ACC) core, increasing to 0.9 in quiescent regions (Haus-  
 246 mann et al., 2017). However, these estimates are limited by the scale of ERA-I reanal-  
 247 ysis ( $0.75 \times 0.75^\circ$ ) and do not isolate coherent eddies. Although the modelled large-amplitude  
 248 eddies used in Fig. 2 are mostly found in WBCs (Fig. 1), our estimate suggests that  $T_{air}$   
 249 adjustments drop further below 0.5 over coherent mesoscale eddies.

250 The value of  $\alpha_A$  ( $\sim 45 \text{ W m}^{-2} \text{ K}^{-1}$ , Fig. 2D) can now be explained by combining  
 251 estimates of  $\lambda_A$  and  $\delta$  using Eq. (7):  $\alpha_A \simeq (1 - 0.32) \times 65.5 \simeq 45 \text{ W m}^{-2} \text{ K}^{-1}$ . As most  
 252 large-amplitude eddies are found in the WBCs, our modelled estimate of  $\alpha_A$  agrees well  
 253 with previous observational estimates of  $40\text{-}56 \text{ W m}^{-2} \text{ K}^{-1}$  in the Kuroshio region and  
 254  $40 \text{ W m}^{-2} \text{ K}^{-1}$  in the Gulf Stream (Hausmann et al., 2016; Ma et al., 2015). Finally,  
 255 the THFF on the prognostic SST,  $\alpha_O$ , is about 10% smaller than  $\alpha_A$  at about  $40 \text{ W m}^{-2} \text{ K}^{-1}$   
 256 (Fig. 2E). The reduction reflects the 10% decrease in the amplitude of mesoscale SST  
 257 anomalies brought by the SST regriding ( $R_g \simeq 0.9$ , see Eq. (8); Fig. 2C).

258 Fig. 3A presents variations of  $\alpha_A$  and  $\alpha_O$  as a function of eddy amplitude  $A$  in N512-  
 259 12. To first order, the THFF increases with eddy amplitude (and hence SST anomalies,  
 260 see Fig. S1). From a minimum of  $\sim 34 \text{ W m}^{-2} \text{ K}^{-1}$  at  $5 \pm 0.05 \text{ cm}$ ,  $\alpha_A$  increases to  $40\text{-}$   
 261  $45 \text{ W m}^{-2} \text{ K}^{-1}$  at  $34 \pm 6 \text{ cm}$  and to  $\sim 40 \text{ W m}^{-2} \text{ K}^{-1}$  on the smallest amplitudes ( $1\text{-}3 \pm 0.05 \text{ cm}$ ).  
 262 Referring to Eq. (7), variations in  $\alpha_A$  are mainly driven by changes in the THF restor-  
 263 ing  $\lambda_A$  whilst the atmospheric adjustment  $\delta$  is relatively insensitive to eddy amplitude  
 264 (compare Fig. S3 D and E). Variations in  $\alpha_O$  follow those of  $\alpha_A$  except at the smallest  
 265 amplitudes where  $R_g$  decreases from 0.9 to about 0.7 (Fig 3D in purple for N512-12).

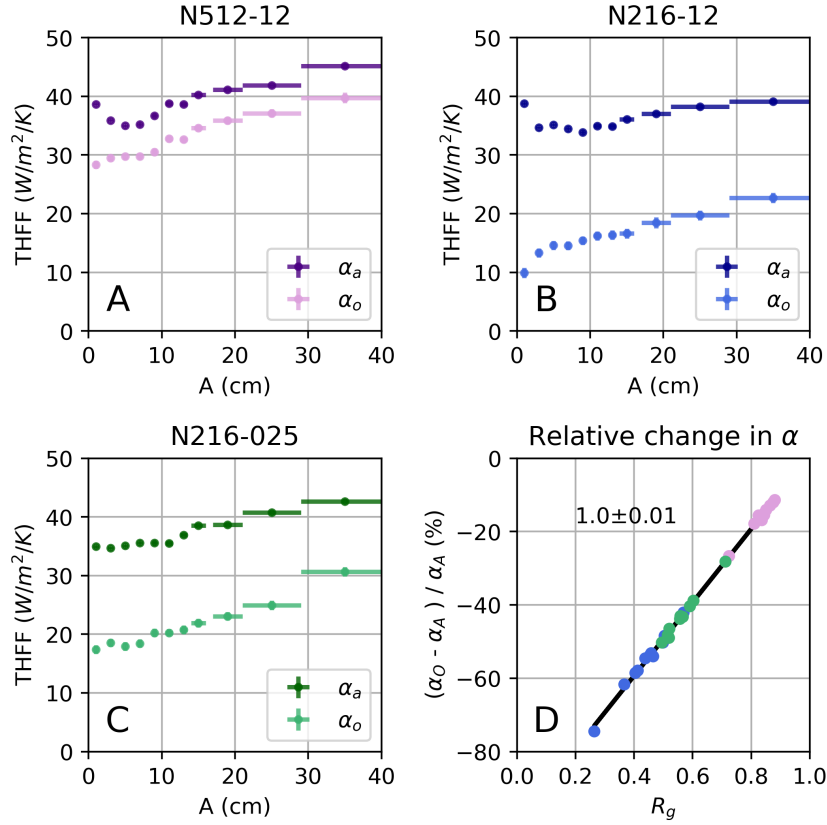


**Figure 3.** THFF  $\alpha_A$  and  $\alpha_O$  as a function of the eddy amplitude (in cm) for N512-12 (subplot A), N216-12 (B) and N216-025 (C), as indicated in the titles. The horizontal bars indicate the width of the eddy amplitude bins, and the vertical error bars indicate 95% confidence intervals. The relative change between  $\alpha_O$  and  $\alpha_A$  (in %) (subplot D) is shown as a function of  $R_g$  for all eddy amplitudes and all model configurations. The gradient of the linear regression line is added as text, to be compared with the theoretical slope of 1 – see Eq. (8).

266

### 3.2 Impact of the ratio of ocean-atmosphere resolution on THFF

267

268

269

270

271

272

273

274

Fig. 3 summarizes estimates of  $\alpha_A$  and  $\alpha_O$  for all configurations and eddy amplitudes. Variations of  $\alpha_A$  are very similar across configurations. This is not surprising as  $\alpha_A$  depends on quantities evaluated on the atmospheric grid: the bulk formulae through  $\lambda_A$  (which are the same in all configurations) and the atmospheric adjustment  $\delta$  which directly 'feels'  $SST_A$  (Eq. 7). In contrast,  $\alpha_O$  varies greatly depending on the mismatch between grid resolutions in ocean and atmosphere.  $\alpha_O$  is biased low relative to  $\alpha_A$  by about 5, 15, and 20  $\text{W m}^{-2} \text{K}^{-1}$  in N512-12, N216-025 and N216-12, respectively. In N216-12, the low bias increases to 25-30  $\text{W m}^{-2} \text{K}^{-1}$  for the small amplitude eddies ( $<5$  cm).

275 Across all configurations and eddy amplitudes, the relative change between  $\alpha_O$  and  
 276  $\alpha_A$  exhibits a strong linear correlation with the regriding parameter  $R_g$ , with a slope  
 277 of 1 as expected from Eq. (8) (Fig. 3D). This reinforces our interpretation that the re-  
 278 griding of SST (captured by  $R_g$ ) plays a fundamental role in determining  $\alpha_O$ 's low bi-  
 279 ases. The difference between  $\alpha_O$  and  $\alpha_A$  increases with  $R_g$  from -15-20% for N512-12,  
 280 to -40-50% for N216-025 and to -50-75% for N216-12. Crucially, the low bias is the largest  
 281 for the smaller amplitude eddies, which cover most of the global ocean, in the configu-  
 282 ration with the largest ratio between atmospheric and oceanic resolutions: N216-12. For  
 283 the small amplitude eddies in N216-12, eddy spatial scale ( $L_{eff} \sim 40$  km) is smaller than  
 284 the atmospheric grid-scale ( $\sim 60$  km). However in N512-12, the scale of small amplitude  
 285 eddies ( $L_{eff} \sim 40$  km) is larger than the atmospheric grid-scale ( $\sim 25$  km), resulting in  
 286 a minimal distortion from  $SST_O$  to  $SST_A$  (Fig. 3A). Regriding of  $SST_O$  reduces the  
 287 amplitude of the mesoscale SST anomalies and creates a spatial shift between  $SST_O$  and  
 288  $SST_A$  (Fig. S). As the heat fluxes are computed from  $SST_A$ , this creates a spatial mis-  
 289 match between the heat flux damping and the prognostic SST,  $SST_O$ .

## 290 4 Conclusions

291 Turbulent heat flux feedbacks over coherent mesoscale eddies are estimated glob-  
 292 ally in three configurations of a high-resolution coupled model HadGEM3-GC3.1. First,  
 293 for the highest ocean-atmosphere resolution available (where the impact of SST regrid-  
 294 ding from the ocean grid to the atmosphere grid is minimal), the modelled estimates of  
 295 the THFF over mesoscale eddies are approximately 35-45 W m<sup>-2</sup> K<sup>-1</sup> depending on eddy  
 296 amplitude. This is the first time this estimate has been provided as previous studies did  
 297 not resolve such small scales nor attempted to isolate coherent eddies. Second, we in-  
 298 vestigate configurations with larger mismatch between oceanic and atmospheric resolu-  
 299 tions. We find that the regriding of SST from the ocean to atmosphere grid results in  
 300 an underestimate of the eddy-induced THFF ranging from 10 to 75%. Importantly, this  
 301 low bias increases with the ratio between atmospheric and ocean resolutions, implying  
 302 that increasing the oceanic resolution at constant atmospheric resolution can actually  
 303 degrade the solution, at least in the representation of air-sea feedbacks.

304 The low bias in the  $\alpha_O$  feedback suggests that eddy SST anomalies are not damp-  
 305 ened enough in the model. The importance of correctly simulating the THFF over mesoscale  
 306 eddies is fundamental in order to represent realistic mesoscale SST anomalies within ed-  
 307 dies and to replicate their interaction with the local and large-scale atmosphere, as well  
 308 as the feedback onto the eddy itself. Even small-amplitude ( $\sim 1$  cm) eddies found across  
 309 the open ocean have a strong THFF between 35-40 W m<sup>-2</sup> K<sup>-1</sup> emphasising the im-

310 portance of transient eddies outside the eddy-rich WBCs and the ACC. Although eddy-  
311 induced THFF can influence the upper-ocean heat budget and weaken thermal strati-  
312 fication (Shan et al., 2020), further work is needed to understand its impact on large-  
313 scale ocean circulation, and its feedback on eddy lifetime.

314 There is considerable variation (up to 40%) between different simulations of mesoscale  
315 air-sea exchanges in high-resolution coupled models and our study is limited to one model  
316 (Yang et al., 2018). Note that the time evolution of the atmospheric adjustment is not  
317 explored, which is likely to affect the THFF strength (Frankignoul et al., 1998; Haus-  
318 mann et al., 2017). Finally, this study focuses on horizontal resolution but changes in  
319 the vertical resolution, in both the ocean and atmosphere, is likely to impact the rep-  
320 resentation of mesoscale eddy-induced SST anomalies and overlying atmospheric adjust-  
321 ment.

322 The results in this study hold implications for future model development. Similarly  
323 to HadGEM3-GC3.1, many current high-resolution coupled models (e.g. HighResMIP)  
324 compute air-sea turbulent heat fluxes on the atmospheric grid, using regridded SST (M. J. Roberts  
325 et al., 2019; Valcke et al., 2015). For the long spin-ups needed for climate simulations,  
326 it is unrealistic to expect the atmospheric resolution to match the oceanic resolution. In-  
327 stead, it is advised when fully resolving mesoscale air-sea exchanges, that air-sea heat  
328 fluxes should be calculated on the finer-scale oceanic grid, as done by the Community  
329 Earth System Model (see Yang et al. (2018)). This method ensures at least that the high-  
330 resolution SST anomalies are maintained. In ocean-only models, the ocean component  
331 is driven through bulk formulae and prescribed surface atmospheric fields, i.e. without  
332 ABL adjustment (i.e.  $\delta = 0$ ). In such setups, we expect mesoscale THFF to approach  
333  $\lambda_A$ . However, the absence of an ABL adjustment also influences  $\lambda_A$  (e.g. neglecting the  
334 effect of dynamical adjustment on the drag coefficient). The net effect of these assump-  
335 tions on the mesoscale THFF in ocean-only models remains to be quantified.

### 336 **Acknowledgments**

337 S. Moreton is funded by the NERC CASE Studentship, UK (NE/N008448/1) and the  
338 Met Office CASE studentship, UK. Met Office authors were supported by the Joint UK  
339 BEIS/Defra Met Office Hadley Centre Climate Programme (GA01101). M. Roberts ac-  
340 knowledges funding received from the European Commission under Grant Agreement  
341 641727 (PRIMAVERA project) of the Horizon 2020 research programme. There are no  
342 conflicts of interest for the authors.

343 **5 Data Availability statement**

344 HighResMIP model data used in this study is freely available from the Earth Sys-  
345 tem Grid Federation (ESGF), <https://esgf-index1.ceda.ac.uk/search/primavera-ceda/>.  
346 The N512-12 configuration datasets (HadGEM3-GC31-HH) are available here: M. Roberts  
347 (2018). The N216-12 configuration datasets (HadGEM3-GC31-MH) are available here:  
348 M. Roberts (2017a). The N216-025 configuration datasets (HadGEM3-GC31-MM) are  
349 available here: M. Roberts (2017b). A dataset of the tracked mesoscale eddies (and their  
350 properties) is freely available here (Moreton & Roberts, 2021) in a repository, under a  
351 Creative Commons Attribution 4.0 International Licence: <https://creativecommons.org/licenses/by/4.0/>.  
352 The 1-yr of data chosen for this study is given in the supplemental material.

## References

- Bishop, S. P., Small, R. J., & Bryan, F. O. (2020). The Global Sink of Available Potential Energy by Mesoscale Air-Sea Interaction. *Journal of Advances in Modeling Earth Systems*. doi: 10.1029/2020ms002118
- Bretherton, F. P. (1982). Ocean climate modeling. *Progress in Oceanography*, 11(2), 93–129. doi: 10.1016/0079-6611(82)90005-2
- Chelton, D. B. (2013). Ocean–atmosphere coupling: Mesoscale eddy effects. *Nature Geoscience*, 6(8), 594–595. Retrieved from <http://www.nature.com/doi/10.1038/ngeo1906> doi: 10.1038/ngeo1906
- Chelton, D. B., Schlax, M. G., & Samelson, R. M. (2011). Global observations of nonlinear mesoscale eddies. *Progress in Oceanography*, 91, 167 – 216. doi: 10.1016/j.pocean.2011.01.002
- Cronin, M. F., Gentemann, C. L., Edson, J., Ueki, I., Bourassa, M., Brown, S., . . . Zhang, D. (2019). Air-Sea Fluxes With a Focus on Heat and Momentum. *Frontiers in Marine Science*, 6(July). doi: 10.3389/fmars.2019.00430
- Ducet, N., Le Traon, P. Y., & Reverdin, G. (2000). Global high-resolution mapping of ocean circulation from TOPEX/Poseidon and ERS-1 and -2. *Journal of Geophysical Research: Oceans*, 105(C8), 19477–19498. doi: 10.1029/2000jc900063
- Frankignoul, C. (1985). Sea Surface Temperature Anomalies, Planetary Waves,. *Reviews of Geophysics*, 23(4), 357–390.
- Frankignoul, C., Czaja, A., & L’Heveder, B. (1998). Air-sea feedback in the North Atlantic and surface boundary conditions for ocean models. *Journal of Climate*, 11(9), 2310–2324. doi: 10.1175/1520-0442(1998)011<2310:ASFITN>2.0.CO;2
- Frankignoul, C., Kestenare, E., Botzet, M., Carril, A. F., Drange, H., Pardaens, A., . . . Sutton, R. (2004). An intercomparison between the surface heat flux feedback in five coupled models, COADS and the NCEP reanalysis. *Climate Dynamics*, 22(4), 373–388. doi: 10.1007/s00382-003-0388-3
- Frenger, I., Gruber, N., Knutti, R., & Münnich, M. (2013). Imprint of Southern Ocean eddies on winds, clouds and rainfall. *Nature Geoscience Letters*, 6, 608 – 612. doi: 10.1038/NGEO1863
- Gregory, J. M., Ingram, W. J., Palmer, M. A., Jones, G. S., Stott, P. A., Thorpe, R. B., . . . Williams, K. D. (2004). A new method for diagnosing radiative forcing and climate sensitivity. *Geophysical Research Letters*, 31(3), 2–5. doi: 10.1029/2003GL018747
- Haarsma, R. J., Roberts, M. J., Vidale, P. L., Catherine, A., Bellucci, A., Bao, Q.,

- 390 ... Von Storch, J. S. (2016). High Resolution Model Intercomparison Project  
 391 (HighResMIP v1.0) for CMIP6. *Geoscientific Model Development*, 9(11),  
 392 4185–4208. doi: 10.5194/gmd-9-4185-2016
- 393 Hausmann, U., & Czaja, A. (2012). The observed signature of mesoscale eddies in  
 394 sea surface temperature and the associated heat transport. *Deep-Sea Research*  
 395 *Part I: Oceanographic Research Papers*, 70, 60–72. Retrieved from <http://dx>  
 396 [.doi.org/10.1016/j.dsr.2012.08.005](https://doi.org/10.1016/j.dsr.2012.08.005) doi: 10.1016/j.dsr.2012.08.005
- 397 Hausmann, U., Czaja, A., & Marshall, J. (2016). Estimates of air-sea feedbacks on  
 398 sea surface temperature anomalies in the Southern Ocean. *Journal of Climate*,  
 399 29(2), 439–454. doi: 10.1175/JCLI-D-15-0015.1
- 400 Hausmann, U., Czaja, A., & Marshall, J. (2017). Mechanisms controlling the SST  
 401 air-sea heat flux feedback and its dependence on spatial scale. *Climate Dynam-*  
 402 *ics*, 48(3-4), 1297–1307. doi: 10.1007/s00382-016-3142-3
- 403 Hayes, S. P., McPhaden, M. J., & Wallace, J. M. (1989). The influence of Sea Sur-  
 404 face Temperature on Surface Wind in the Eastern Equatorial Pacific: Weekly  
 405 to Monthly Variability. *Journal of Climate*, 2, 1500–1506.
- 406 Hewitt, H. T., Bell, M. J., Chassignet, E. P., Czaja, A., Ferreira, D., Griffies, S. M.,  
 407 ... Roberts, M. J. (2017). *Will high-resolution global ocean models bene-*  
 408 *fit coupled predictions on short-range to climate timescales?* (Vol. 120). doi:  
 409 10.1016/j.ocemod.2017.11.002
- 410 Hewitt, H. T., Copsey, D., Culverwell, I. D., Harris, C. M., Hill, R. S., Keen, A. B.,  
 411 ... Hunke, E. C. (2011). Design and implementation of the infrastructure of  
 412 HadGEM3: The next-generation Met Office climate modelling system. *Geosci-*  
 413 *entific Model Development*, 4(2), 223–253. doi: 10.5194/gmd-4-223-2011
- 414 Hogg, A. M., Dewar, W. K., Berloff, P., Kravtsov, S., & Hutchinson, D. K. (2009).  
 415 The effects of mesoscale ocean-atmosphere coupling on the large-scale ocean  
 416 circulation. *Journal of Climate*. doi: 10.1175/2009JCLI2629.1
- 417 Jullien, S., Masson, S., Oerder, V., Samson, G., Colas, F., & Renault, L. (2020).  
 418 Impact of ocean-atmosphere current feedback on ocean mesoscale activity:  
 419 Regional variations and sensitivity to model resolution. *Journal of Climate*,  
 420 33(7), 2585–2602. doi: 10.1175/JCLI-D-19-0484.1
- 421 Large, W., & Yeager, S. (2004). Diurnal to Decadal Global Forcing The Data  
 422 Sets and Flux Climatologies. *NCAR Tech. Note*(2004), 1–105. doi:  
 423 10.5065/D6KK98Q6
- 424 Leyba, I. M., Saraceno, M., & Solman, S. A. (2016). Air-sea heat fluxes associated  
 425 to mesoscale eddies in the Southwestern Atlantic Ocean and their dependence  
 426 on different regional conditions. *Climate Dynamics*, 49(7-8), 2491–2501. doi:

- 427 10.1007/s00382-016-3460-5
- 428 Li, F., Sang, H., & Jing, Z. (2017). Quantify the continuous dependence of SST-  
429 turbulent heat flux relationship on spatial scales. *Geophysical Research Letters*,  
430 *44*(12), 6326–6333. doi: 10.1002/2017GL073695
- 431 Ma, X., Chang, P., Saravanan, R., Montuoro, R., Hsieh, J., Wu, D., . . . Jing, Z.  
432 (2015). Distant Influence of Kuroshio Eddies on North Pacific Weather Pat-  
433 terns ? *Nature: Scientific Reports*.
- 434 Ma, X., Jing, Z., Chang, P., Liu, X., Montuoro, R., Small, R. J., . . . Wu, L.  
435 (2016). Western boundary currents regulated by interaction between  
436 ocean eddies and the atmosphere. *Nature*, *535*(7613), 533–537. Retrieved  
437 from <http://www.nature.com/doi/10.1038/nature18640> doi:  
438 10.1038/nature18640
- 439 Madec, G. (2008). NEMO ocean engine. *Note du Pôle de modélisation, Institut*  
440 *Pierre-Simon Laplace (IPSL), France*(27), 1 – 396.
- 441 Mason, E., Pascual, A., & McWilliams, J. C. (2014). A new sea surface height-based  
442 code for oceanic mesoscale eddy tracking. *Journal of Atmospheric and Oceanic*  
443 *Technology*, *31*(5), 1181–1188. doi: 10.1175/JTECH-D-14-00019.1
- 444 Minobe, S., Kuwano-Yoshida, A., Komori, N., Xie, S. P., & Small, R. J. (2008).  
445 Influence of the Gulf Stream on the troposphere. *Nature*, *452*(7184), 206–209.  
446 doi: 10.1038/nature06690
- 447 Moreton, S. M., Ferreira, D., Roberts, M., & Hewitt, H. (2020). Evaluat-  
448 ing surface eddy properties in coupled climate simulations with ‘eddy-  
449 present’ and ‘eddy-rich’ ocean resolution. *Ocean Modelling*, *147*. doi:  
450 10.1016/j.ocemod.2020.101567
- 451 Moreton, S. M., & Roberts, M. (2021). *An eddy tracking dataset for N512-12, N216-*  
452 *12 and N216-025 model configurations of HadGEM3-GC3.1*. Retrieved from  
453 <https://researchdata.reading.ac.uk/id/eprint/283> doi: [http://dx.doi](http://dx.doi.org/10.17864/1947.283)  
454 [.org/10.17864/1947.283](http://dx.doi.org/10.17864/1947.283).
- 455 Putrasahan, D. A., Miller, A. J., & Seo, H. (2013). Isolating mesoscale coupled  
456 ocean-atmosphere interactions in the Kuroshio Extension region. *Dynamics of*  
457 *Atmospheres and Oceans*, *63*, 60–78. Retrieved from [http://dx.doi.org/10](http://dx.doi.org/10.1016/j.dynatmoce.2013.04.001)  
458 [.1016/j.dynatmoce.2013.04.001](http://dx.doi.org/10.1016/j.dynatmoce.2013.04.001) doi: 10.1016/j.dynatmoce.2013.04.001
- 459 Rahmstorf, S., & Willebrand, J. (1995). The Role of Temperature Feedback in Sta-  
460 bilizing the Thermocline Circulation. *Journal of Physical Oceanography*, *25*,  
461 787–805.
- 462 Renault, L., Marchesiello, P., Masson, S., & McWilliams, J. C. (2019). Remarkable  
463 Control of Western Boundary Currents by Eddy Killing, a Mechanical Air-

- 464 Sea Coupling Process. *Geophysical Research Letters*, 46(5), 2743–2751. doi:  
465 10.1029/2018GL081211
- 466 Renault, L., Molemaker, M. J., McWilliams, J. C., Shchepetkin, A. F., Lemarié, F.,  
467 Chelton, D. B., ... Hall, A. (2016). Modulation of Wind-Work by Oceanic  
468 Current Interaction with the Atmosphere. *Journal of Climate*, 46, 1685 –  
469 1703. doi: 10.1175/JPO-D-15-0232.1
- 470 Roberts, M. (2017a). *MOHC HadGEM3-GC31-MH model output prepared for*  
471 *CMIP6 HighResMIP. Version 20190901*. Retrieved from [http://doi.org/10](http://doi.org/10.22033/ESGF/CMIP6.1762)  
472 [.22033/ESGF/CMIP6.1762](http://doi.org/10.22033/ESGF/CMIP6.1762) doi: <http://doi.org/10.22033/ESGF/CMIP6.1762>
- 473 Roberts, M. (2017b). *MOHC HadGEM3-GC31-MM model output prepared for*  
474 *CMIP6 HighResMIP Version 20190901*. Retrieved from [http://doi.org/10](http://doi.org/10.22033/ESGF/CMIP6.1902)  
475 [.22033/ESGF/CMIP6.1902](http://doi.org/10.22033/ESGF/CMIP6.1902) doi: <http://doi.org/10.22033/ESGF/CMIP6.1902>
- 476 Roberts, M. (2018). *MOHC HadGEM3-GC31-HH model output prepared for CMIP6*  
477 *HighResMIP Version 20190901*. Retrieved from [http://doi.org/10.22033/](http://doi.org/10.22033/ESGF/CMIP6.445)  
478 [ESGF/CMIP6.445](http://doi.org/10.22033/ESGF/CMIP6.445) doi: <http://doi.org/10.22033/ESGF/CMIP6.445>
- 479 Roberts, M. J., Baker, A., Blockley, E. W., Calvert, D., Coward, A., Hewitt, H. T.,  
480 ... Vidale, P. L. (2019). Description of the resolution hierarchy of the global  
481 coupled HadGEM3-GC3.1 model as used in CMIP6 HighResMIP experi-  
482 ments. *Geoscientific Model Development Discussions*, 12, 4999–5028. doi:  
483 10.5194/gmd-2019-148
- 484 Roberts, M. J., Hewitt, H. T., Hyder, P., Ferreira, D., Josey, S. A., Mizielinski, M.,  
485 & Shelly, A. (2016). Impact of ocean resolution on coupled air-sea fluxes and  
486 large-scale climate. *Geophysical Research Letters*, 43(19), 10,430–10,438. doi:  
487 10.1002/2016GL070559
- 488 Seo, H., Miller, A. J., & Norris, J. (2016). Eddy – Wind Interaction in the Cali-  
489 fornia Current System: Dynamics and Impacts. *Journal of Physical Oceanogra-*  
490 *phy*, 46(1989), 439–459. doi: 10.1175/JPO-D-15-0086.1
- 491 Shan, X., Jing, Z., Gan, B., Wu, L., Chang, P., Ma, X., & Wang, S. (2020). Surface  
492 Heat Flux Induced by Mesoscale Eddies Cools the Kuroshio - Oyashio Exten-  
493 sion Region. *Geophysical Research Letters*, 1–9. doi: 10.1029/2019GL086050
- 494 Small, R. J., Bryan, F. O., Bishop, S. P., Larson, S., & Tomas, R. A. (2020).  
495 What drives upper-ocean temperature variability in coupled climate mod-  
496 els and observations? *Journal of Climate*, 33(2), 577–596. doi: 10.1175/  
497 JCLI-D-19-0295.1
- 498 Small, R. J., Bryan, F. O., Bishop, S. P., & Tomas, R. A. (2019). Air-sea tur-  
499 bulent heat fluxes in climate models and observational analyses: What  
500 drives their variability? *Journal of Climate*, 32(8), 2397–2421. doi:

- 501 10.1175/JCLI-D-18-0576.1
- 502 Small, R. J., DeSzoek, S. P., Xie, S. P., O'Neill, L., Seo, H., Song, Q., ... Minobe,  
503 S. (2008). Air-sea interaction over ocean fronts and eddies. *Dynamics of Atmo-*  
504 *spheres and Oceans*, 45(3-4), 274–319. doi: 10.1016/j.dynatmoce.2008.01.001
- 505 Storkey, D., Blaker, A. T., Mathiot, P., Megann, A., Aksenov, Y., Blockley, E. W.,  
506 ... Sinha, B. (2018). UK Global Ocean GO6 and GO7: a traceable hierarchy  
507 of model resolutions. *Geoscientific Model Development*, 11(8), 3187–3213. Re-  
508 trieved from <https://www.geosci-model-dev-discuss.net/gmd-2017-263/>  
509 doi: 10.5194/gmd-2017-263
- 510 Valcke, S. (2013). The OASIS3 coupler: a European climate modelling community  
511 software. *Geoscientific Model Development*, 6(2), 373–388. Retrieved from  
512 <http://www.geosci-model-dev.net/6/373/2013/> doi: 10.5194/gmd-6-373  
513 -2013
- 514 Valcke, S., Craig, T., & L., C. (2015). OASIS3-MCT User Guide. *OASIS3-MCT*  
515 *3.0, Technical Report, TR/CMGC/15/38, CER- FACS/CNRS SUC URA No.*  
516 *1875*, (May).
- 517 Villas Bôas, A. B., Sato, O. T., Chaigneau, A., & Castelão, G. P. (2015). The  
518 signature of mesoscale eddies on the air-sea turbulent heat fluxes in the  
519 South Atlantic Ocean. *Geophysical Research Letters*, 42(6), 1856–1862. doi:  
520 10.1002/2015GL063105
- 521 Wallace, J. M., Mitchell, T. P., & Deser, C. (1989). *The Influence of Sea-*  
522 *Surface Temperature on Surface Wind in the Eastern Equatorial Pacific:*  
523 *Seasonal and Interannual Variability* (Vol. 2) (No. 12). doi: 10.1175/  
524 1520-0442(1989)002<1492:tiosst>2.0.co;2
- 525 Walters, D., Boutle, I., Brooks, M., Melvin, T., Stratton, R., Vosper, S., ... Xavier,  
526 P. (2017). The Met Office Unified Model Global Atmosphere 6.0/6.1 and  
527 JULES Global Land 6.0/6.1 configurations. *Geoscientific Model Development*,  
528 10, 1487–1520. doi: 10.5194/gmd-10-1487-2017
- 529 Williams, K. D., Copsey, D., Blockley, E. W., Bodas-Salcedo, A., Calvert, D.,  
530 Comer, R., ... Xavier, P. K. (2018). The Met Office Global Coupled Model  
531 3.0 and 3.1 (GC3.0 and GC3.1) Configurations. *Journal of Advances in Model-*  
532 *ing Earth Systems*, 10(2), 357–380. doi: 10.1002/2017MS001115
- 533 Xie, S. P. (2004). *Satellite observations of cool ocean-atmosphere interaction*  
534 (Vol. 85) (No. 2). doi: 10.1175/bams-85-2-195
- 535 Yang, P., Jing, Z., & Wu, L. (2018). An Assessment of Representation of Oceanic  
536 Mesoscale Eddy-Atmosphere Interaction in the Current Generation of General  
537 Circulation Models and Reanalyses. *Geophysical Research Letters*, 45(21),

